ChemComm

COMMUNICATION

View Article Online
View Journal | View Issue

Cite this: *Chem. Commun.*, 2025, **61**, 11633

Received 4th June 2025,
Accepted 23rd June 2025

DOI: 10.1039/d5cc03179f

rsc.li/chemcomm

A carbazole-embedded cyclodimer adopting a helical conformation and metal-ion sensing†

Athira Naniyil, Arun Kumar, Aathira Edwin and Sabapathi Gokulnath *

An unprecedented formation of carbazole-embedded decaphyrin through acid-catalyzed condensation of appropriate coupling partners is reported. Single crystal X-ray diffraction analysis revealed that the macrocycle adopted a 'figure-of-eight' structure, wherein two pyrrole and thiophene rings were inverted. The absorption spectrum of the macrocycle exhibited ill-defined bands and it shows specific affinity towards soft metal ions such as Ag^{+} and Hg^{2+}.

Porphyrinoid scaffolds remain a focal point of interest for the synthetic community, owing to their broad spectrum of applications spanning from medicine to materials chemistry.[1,2] Among these, modified porphyrinoids have emerged as exceptional sensing materials, due to their unique structural and electronic properties.[3,4] These macrocycles feature a highly conjugated π-system, making them excellent candidates for interacting with various analytes through π–π stacking, hydrogen bonding, or metal coordination.[5] The ability of porphyrins to coordinate with a wide range of metal ions further enhances their application as selective and sensitive sensors for environmental, biological, and chemical detection. Additionally, their strong optical absorption in the visible and UV regions, along with fluorescence properties, enables them to be used in spectroscopic-based detection techniques.[6] Modifications to the porphyrin framework, such as functional group or heteroatom incorporation, allow distinct sensing properties for specific ions.[7] As a result, porphyrins and related macrocycles have been utilized in detecting gases, metal ions, organic molecules, and biological entities, demonstrating their potential in the field of environmental monitoring, medical diagnostics, and industrial quality control.[8]

Expanded porphyrins have been widely studied due to their appealing characteristics, such as large, flexible, and versatile structures, adaptable electronic properties that support the formation of diverse conformations, multiple electronic states, rich coordination chemistry, anion/cation binding capabilities, and substantial two-photon absorption cross sections.[9–11] The first decaphyrin, [40]turcasarin reported by Sessler and co-workers, turned out to be nonaromatic exhibiting a helical conformation.[12] Subsequently, an aromatic decaphyrin showed a large two-photon absorption (TPA) cross-section, highlighting its potential for nonlinear optical applications.[13] Further advancements include the synthesis of *meso*-aryl and alkyl-substituted decaphyrins, which upon metalation led to stable organic π-radicals.[14,15] Later, Osuka and co-workers employed a rational design strategy to generate a series of decaphyrins incorporating phenylene and thienyl bridges.[16,17] More recently, Ravikanth's group developed dibenzidecaphyrins and their bis-BF_2 complexes exhibiting 'figure-of-eight' conformations.[18]

To date, a large number of expanded porphyrins have been reported wherein carbazole is used as a building block.[19] In 2021, our group reported planar carbazole-based hexaphyrin-like macrocycles with bis-coordinating cores (**A**), which led to box-shaped and excitonically coupled cyclic bis-BODIPYs.[20] In the same year, Lei and co-workers demonstrated a pair of *meso*-unsubstituted expanded carbaporphyrins containing two carbazole moieties with 'figure-of-eight' conformation (**B**) that undergo protonation-triggered conformational changes.[21] In 2022, the same group exploited the coordination chemistry of **B** and obtained a 2 : 1 metal-to-ligand metalloring complex (**C**) along with an expanded 6 : 3 metal-to-ligand metallocage complex.[22] On the other hand, a fully conjugated cryptand-like bicyclic porphyrinoid (**D**), incorporating three carbazole linkages and four dipyrrin subunits was reported, which acts as an effective ligand for multiple BF_2 complexation.[23] Subsequently, Song and co-workers reported a conformationally restricted and a rare three-dimensionally extended carbazole-incorporating expanded porphyrinoids (**E**).[24] More recently, the same group also reported the synthesis of a carbazole-incorporated doubly linked spiro-dimer (**F**)[25] from a [22]smaragdyrins BF_2 complex through an oxidative coupling in the presence of $RuCl_3$ (Fig. 1).

Herein, we aimed to prepare a benzofused sapphyrin-like macrocycle **2** using the [3+2] methodology. However, instead of

School of Chemistry, Indian Institute of Science Education Research Thiruvananthapuram, India. E-mail: gokul@iisertvm.ac.in

† Electronic supplementary information (ESI) available. CCDC 2429004. For ESI and crystallographic data in CIF or other electronic format see DOI: https://doi.org/10.1039/d5cc03179f

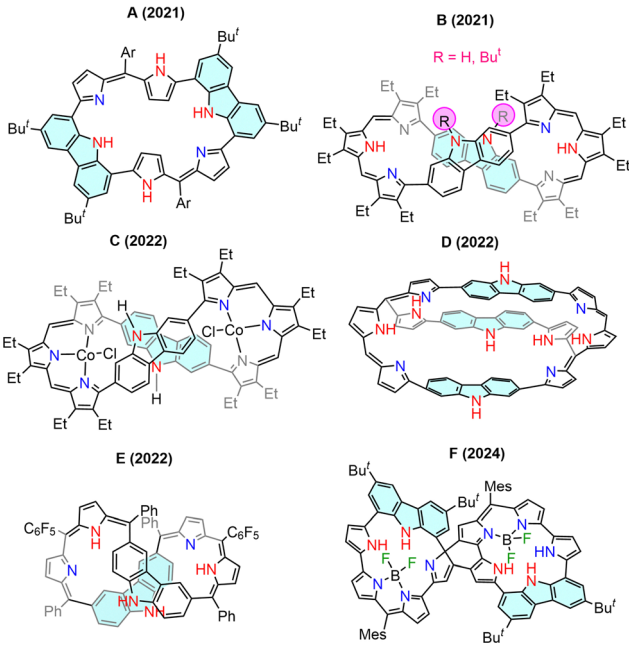

Fig. 1 Previously reported carbazole-incorporated expanded macrocycles (A–F).

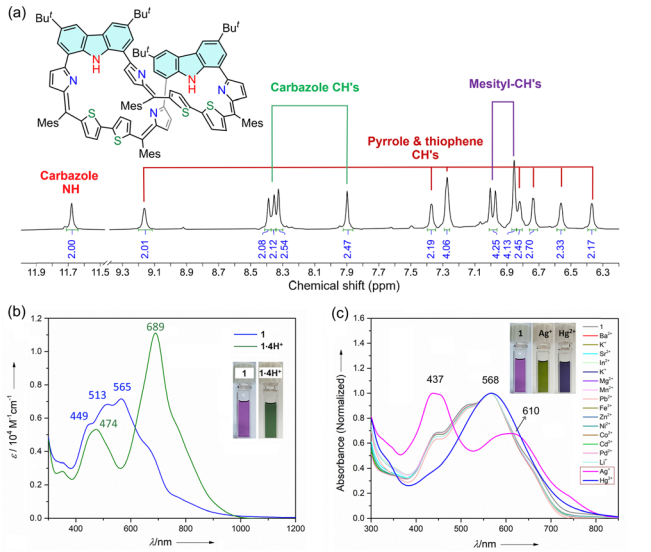

Fig. 2 (a) ^{1}H NMR spectrum of macrocycle 1 in CD_2Cl_2 at 298 K. The selected region is shown. (*) denotes residual CH_2Cl_2 signal. UV/Vis absorption spectra of (b) 1 and **1·4H$^+$** and (c) UV-Vis absorption changes of 1 (in CH_2Cl_2) upon the addition of various metal ions (in CH_3OH).

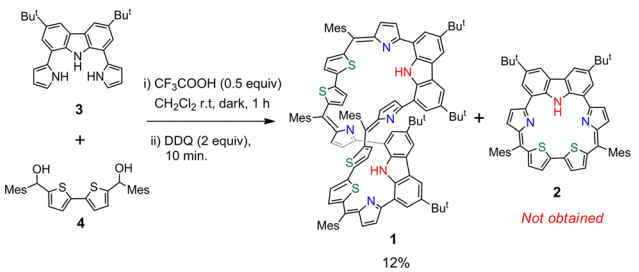

Scheme 1 Synthesis of macrocycle **1**.

2, we have obtained the larger macrocycle **1** resembling a 'figure-of-eight' structure as confirmed by single crystal X-ray structure. Intriguingly, macrocycle **1** showed distinct and instant colour changes upon adding Ag^+ and Hg^{2+} ions substantiated with UV-Vis absorption spectral changes (Fig. 2c). The starting materials **3**[26] (prepared from carbazole in 42% overall yield) and **4**[27] (prepared from thiophene in 35% overall yield) were synthesized by following the literature procedure. With these in the background, we went on to synthesize carbazole-based decaphyrin using the key building block reported earlier.[28] The expanded carbazole-embedded helical macrocycle was obtained in 12% yield *via* acid-catalyzed condensation of **3** and **4** in the presence of trifluoroacetic acid (TFA) followed by 2,3-dichloro-5,6-dicyano-1,4 benzoquinone (DDQ) oxidation (Scheme 1). Sequential basic alumina column followed by silica-gel chromatographic separations were done to obtain the purified macrocycle.

The exact composition of macrocycle **1** was confirmed by using HRMS analysis, which showed a molecular ion peak at m/z = 1663.7432 ([M]$^+$; calcd for: $C_{112}H_{107}N_6S_4$: 1663.7440). The macrocycle **1** was thoroughly characterized by ^{1}H, ^{1}H–^{1}H COSY and ^{1}H–^{1}H ROESY NMR spectral analysis. The ^{1}H NMR spectrum of **1** in CD_2Cl_2 exhibits a C_2 symmetric feature despite the conformational dynamics in solution (Fig. 2a). A broad signal at 11.68 ppm was ascribed to the NH proton of the carbazole ring similar to our previously reported carbazole-based macrocycles.[26,28] Furthermore, the absence of any NH signals, even at low temperature, proved that all the remaining four pyrroles are in iminic form. The β-pyrrolic and β-thiophenic protons resonated between 6.36 to 9.17 ppm. The chemical shift at 9.18 ppm is attributed to one of the β-protons of the thiophene ring, likely due to hydrogen bonding with the adjacent imino-pyrrole nitrogen, as suggested by the crystal structure. This interaction leads to significant deshielding, causing this particular β-proton of the thiophene to appear further downfield compared to other thiophene or pyrrole protons. The signals for *meta* protons of the *meso*-mesityl rings were observed from 6.85 to 7.00 ppm, whereas the peripheral carbazole CHs were observed as four singlets at 7.90, 8.33, 8.37 and 8.39 ppm. The peaks corresponding to the methyl protons from four mesityl groups were observed as six resonances in the upfield region (1.67 to 2.37 ppm) due to its C_2 symmetry in the solution state. A 2D NMR experiment was employed to distinguish the peaks corresponding to pyrrole and thiophene protons, since signals from both these heterocyclic rings showed correlations in the ^{1}H–^{1}H COSY spectrum (Fig. S4-2, ESI†). Variable temperature (VT) NMR of macrocycle **1** recorded from 253 K to 313 K revealed that the signals sharpen and show well-defined splitting patterns upon cooling, while higher temperatures result in broadened signals and less distinct splitting. These observations indicate that the macrocycle exhibits conformational flexibility at room temperature, which becomes restricted at lower temperatures due to slowed dynamic processes.

The UV-Vis absorption spectrum of **1** in CH_2Cl_2 shows ill-defined bands at 276, 449, 513 and 565 nm and covering into

the entire visible region reaching up to 1200 nm (Fig. 2b). Such spectral features are characteristic of non-aromatic nature, presumably due to the disruption in conjugation at the carbazole ring. Upon protonation using diluted CF_3COOH, significant spectral changes were observed such as a two-fold increase in the molar extinction coefficient and bathochromic shift of all the bands associated with appearance at 287, 474 and 689 nm with the low energy absorption tail reaching up to *ca.* 1000 nm. Such changes could be due to the complete protonation of four imino sites (Fig. S4-5, ESI†). Furthermore, we have examined the affinity of **1** with a series of acetate salts of transition-metal ions (Mn^{2+}, Fe^{3+}, Co^{2+}, Ni^{2+}, Cd^{2+}, Zn^{2+}, Pd^{2+}, Ag^{+}, and Hg^{2+}) and some group I (Li^{+}, Na^{+}, and Cs^{+}) and group 2 (Mg^{2+}, Sr^{2+}, and Ba^{2+}) metal ions in alcoholic solution (Fig. 2c). Initial binding studies from UV-Vis absorption revealed that only Ag^{+} and Hg^{2+} caused significant spectral changes. Such binding can be distinguishable by the naked eye with instant colour changes from violet to green for Ag^{+} and violet to blue for Hg^{2+} (Fig. S5-3, ESI†).

UV–Vis spectral studies at room temperature were employed using the continuous variation method (Job's plot) to determine the binding stoichiometry of Ag^{+} and Hg^{2+} ions.[29] Metal ions (in methanol) and macrocycle **1** were mixed in varying proportions, with mole fractions ranging from 0.1 to 0.9 (aliquots of 0.1). The absorbance of the **1-Ag** and **1-Hg** complexes was plotted against the mole fraction of metal ions (Fig. S5-4, ESI†). The inflection points in these plots indicated the mole fraction of metal ions bound to macrocycle **1**. The binding stoichiometry was derived from the intersection points of the two slopes obtained, which occurred at a mole fraction of 0.7 for both Ag^{+} and Hg^{2+}, respectively, which proved the existence of 1 : 2 stoichiometry for the ligand to metal ratio. Furthermore, the formation of both Ag and Hg bound species was confirmed using ESI-MS spectral analysis (Fig. S3-2 and S3-3, ESI†), which is also substantiated with ^{1}H NMR titration experiments with the disappearance of NH signals upon metal-ion binding (Fig. S4-6 and S4-7, ESI†).

Further structural proof came from the single crystal X-ray analysis of **1**. The crystals were grown by the slow vapor diffusion of methanol into a solution of a racemic mixture of **1** in THF at room temperature. The structure consists of two carbazole moieties and two bithiophene units connected through four pyrrole bridges affording a 'figure-of-eight' like conformation (Fig. 3a and b). Among these, two pyrrolic nitrogens that are directly linked onto the 8-position of the carbazole ring at the crossover points are orienting outward. In addition, among two bithiophene units, one of the thiophene subunits in each bithiophene is pointing outward from the macrocyclic core, presumably to avoid the steric congestion. The two carbazole units are positioned on the same side of the macrocycle and lie in planes that are almost parallel to each other displaying a parallelogram-like feature through the *ab* axis (Fig. 3b). The 3D crystal packing of **1** reveals a racemic mixture, consisting of enantiomers (*P*,*P*) and (*M*,*M*) arranged in a 1 : 1 ratio (Fig. 3c).[30] We presume that the existence of helical chirality in **1** is due to its 'figure-of-eight' conformation. Therefore, we have attempted to purify the corresponding enantiomers using the chiral column separation technique. However, after several attempts, we were

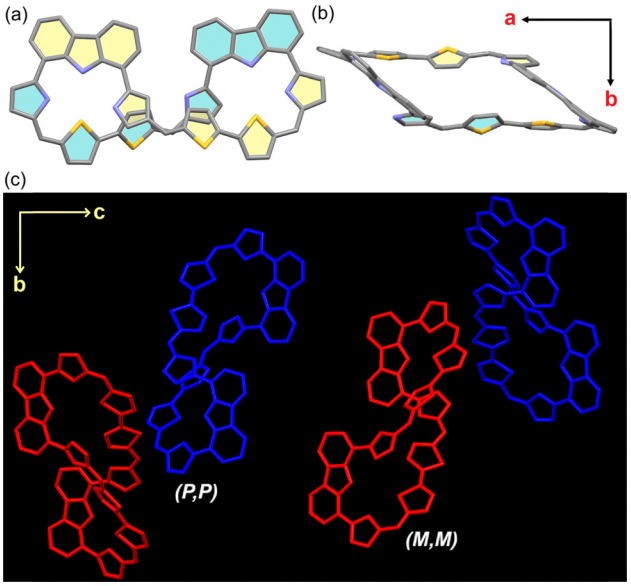

Fig. 3 Crystal structure of **1**. (a) Top view; (b) side view and (c) the 3D crystal packing of **1** showing (*P*,*P*) and (*M*,*M*) enantiomers. *Meso*-aryl, H's and *tert*-butyl groups have been removed for clarity.

unable to obtain the pure enantiomers possibly due to the fast racemization between the (*P*,*P*) and (*M*,*M*) enantiomers of **1**. Hence, we have utilized a chiral acid such as D-(−)-mandelic acid and L-(+)-mandelic acid for the kinetic dynamic resolution of macrocycle **1** (Fig. 4).[31] We envisaged that the chiral acid is protonating one or more imino-pyrrolic subunits present in **1**, thereby transferring the chirality to the entire macrocycle. Hence, the CD spectral features are dominant with the absorption spectral features as that of protonated **1** (Fig. 2b). The two fractions obtained separately upon the addition of **1** D-(−)-mandelic acid and L-(+)-mandelic acid show mirror image cotton effects.

To gain deeper insights into the electronic structures of macrocycle **1** and **1**·**4H**$^+$, DFT calculations were performed using the B3LYP/6-31G(d) level of theory. The ground-state optimized geometry showed the structural parameters for **1** similar to those obtained from the X-ray crystal structure. The analysis of the frontier molecular orbitals for compound **1** reveals that the HOMO is located on the macrocyclic core, encompassing the entire carbazole subunit whereas the LUMO is located mostly on the carbazole units (Fig. 5). The HOMO of the protonated form presents a seemingly uneven distribution of orbital density that was dominant on the carbazole units on either side, but the pyrrole and thiophene units were deficient in prominent orbital density. The LUMO, quite the reverse, exhibits poor orbital overlap of the carbazole units with the rest of the macrocycle and the orbital density was mainly distributed on the pyrrole and thiophene units. The excitation energies and oscillator strengths for the first 50 S_0–S_n transitions were obtained from TD-DFT studies (Tables S7-1 and S7-2, ESI†). The TD-DFT results are closely aligned with the experimentally observed absorption spectrum of macrocycle **1** and **1**·**4H**$^+$ (Fig. S7-6 and S7-7, ESI†). The nucleus-independent chemical shift [NICS (0)] values (−0.52 ppm for **1** and +0.10 ppm for **1**·**4H**$^+$) were computed using optimized structures suggesting

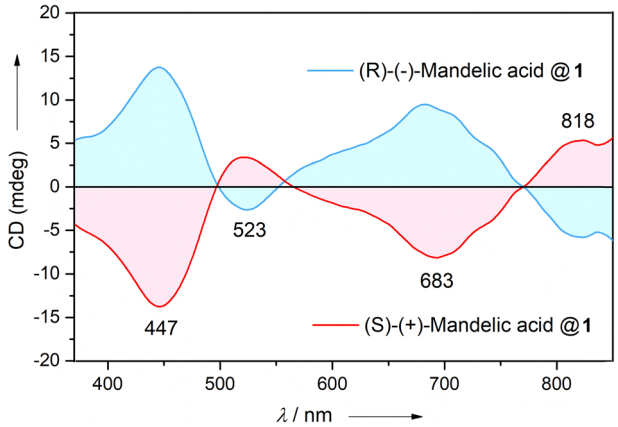

Fig. 4 CD spectra of **1**, in the presence of 50 equiv. of D-(−)-mandelic acid (blue) and L-(+)-mandelic acid (red) in CH_2Cl_2 at 298 K.

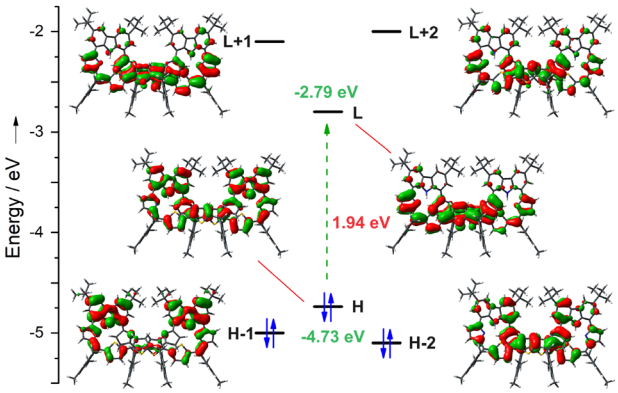

Fig. 5 Energy level diagram along with Kohn–Sham orbitals of **1**.

that these systems are deemed to be nonaromatic (Fig. S7-3, ESI†). This observation is further supported by AICD plots, which show no continuous flow of magnetic vectors in the macrocycle (Fig. S7-2, ESI†).

In summary, a carbazole-embedded decaphyrin **1** was obtained *via* an acid-catalyzed condensation of appropriate precursors. The solution-state structures of **1** and bound metal ions were studied using NMR spectroscopy and the solid-state structure of **1** was unambiguously confirmed using single-crystal X-ray analysis. A parallelogram-like structure can be seen, which adopts a well-known 'figure-of-eight' conformation with two inverted pyrrole and thiophene rings. The specific affinity toward soft metal ions such as Ag^+ and Hg^{2+} ions is deemed to be accompanied by both the HSAB interaction of the thiophenic sulfur and carbazole NHs through deprotonation as evident from NMR and mass spectral results. The same is clearly distinguishable by naked-eye detection along with changes in the optical features. A 1 : 2 stoichiometry for the ligand–metal complexes was obtained using Job's plot. NICS (0) values and ACID plots indicated non-aromaticity due to discontinuous conjugation within the carbazole moiety.

This work was supported by IISER Thiruvananthapuram and SERB Core Research Grant No. EEQ/2023/000756. We thank Alex Andrews for solving the X-ray structure of **1**. A. N. thanks CSIR for her fellowship.

Conflicts of interest

There are no conflicts to declare.

Data availability

The experimental and theoretical data supporting this article have been included as part of the ESI.†

Notes and references

1 Y. Shi, F. Zhang and R. J. Linhardt, *Dyes Pigm.*, 2021, **188**, 109136.
2 F. Yang, M. Xu, X. Chen and Y. Luo, *Biomed. Pharmacother.*, 2023, **164**, 114933.
3 R. Paolesse, S. Nardis, D. Monti, M. Stefanelli and C. Di Natale, *Chem. Rev.*, 2017, **117**, 2517–2583.
4 S. Ishihara, J. Labuta, W. Van Rossom, D. Ishikawa, K. Minami, J. P. Hill and K. Ariga, *Phys. Chem. Chem. Phys.*, 2014, **16**, 9713–9746.
5 G. Singh and S. Chandra, *Electrochem. Sci. Adv.*, 2023, **3**, 1–19.
6 W. Zheng, N. Shan, L. Yu and X. Wang, *Dyes Pigm.*, 2008, **77**, 153–157.
7 A. Kalaiselvan, A. Naniyil, R. M. Ipe, S. V. Krishna Isukapalli, S. R. Vennapusa, A. P. Andrews and S. Gokulnath, *J. Org. Chem.*, 2023, **88**, 14377–14387.
8 K. Norvaiša, M. Kielmann and M. O. Senge, *ChemBioChem*, 2020, **21**, 1793–1807.
9 T. K. Chandrashekar and S. Venkatraman, *Acc. Chem. Res.*, 2003, **36**, 676–691.
10 A. Osuka and S. Saito, *Chem. Commun.*, 2011, **47**, 4330–4339.
11 A. Alka, V. S. Shetti and M. Ravikanth, *Coord. Chem. Rev.*, 2019, **401**, 213063.
12 J. L. Seasler, S. J. Weghorn, V. Lynch and M. R. Johnson, *Angew. Chem., Int. Ed. Engl.*, 1994, **33**, 1509–1512.
13 H. Rath, V. Prabhuraja, T. K. Chandrashekar, A. Nag, D. Goswami and B. S. Joshi, *Org. Lett.*, 2006, **8**, 2325–2328.
14 T. Yoneda, Y. M. Sung, J. M. Lim, D. Kim and A. Osuka, *Angew. Chem., Int. Ed.*, 2014, **53**, 13169–13173.
15 Y. Tanaka, T. Yoneda, K. Furukawa, T. Koide, H. Mori, T. Tanaka, H. Shinokubo and A. Osuka, *Angew. Chem., Int. Ed.*, 2015, **54**, 10908–10911.
16 V. G. Anand, S. Saito, S. Shimizu and A. Osuka, *Angew. Chem., Int. Ed.*, 2005, **44**, 7244–7248.
17 T. Soya, H. Mori, Y. Hong, Y. H. Koo, D. Kim and A. Osuka, *Angew. Chem., Int. Ed.*, 2017, **56**, 3232–3236.
18 S. Kumar, K. G. Thorat and M. Ravikanth, *J. Org. Chem.*, 2018, **83**, 14277–14285.
19 S. Das and I. Gupta, *J. Porphyrins Phthalocyanines*, 2019, **23**, 367–409.
20 A. Kalaiselvan, S. Dhamija, C. Aswathi, A. K. De and S. Gokulnath, *Chem. Commun.*, 2021, **57**, 11485–11488.
21 W. Zhou, M. Hao, T. Lu, Z. Duan, T. Sarma, J. L. Sessler and C. Lei, *Chem. – Eur. J.*, 2021, **27**, 16173–16180.
22 W. Zhou, T. Sarma, Y. Su, C. Lei and J. L. Sessler, *Chem. Sci.*, 2022, **13**, 692–697.
23 W. Zhou, T. Sarma, L. Yang, C. Lei and J. L. Sessler, *Chem. Sci.*, 2022, **13**, 7276–7282.
24 F. Li, K. Wang, Y. Rao, L. Xu, A. Osuka and J. Song, *Org. Chem. Front.*, 2022, **9**, 4798–4802.
25 J. Chen, H. Nie, Y. Rao, L. Xu, M. Zhou, B. Yin, J. Song and A. Osuka, *Chem. – Asian J.*, 2024, **19**, 1–6.
26 A. Naniyil, N. Koroth Valappil, A. P. Andrews and S. Gokulnath, *Chem. Commun.*, 2024, **60**, 6957–6960.
27 A. Srinivasan, V. M. Reddy, S. J. Narayanan, B. Sridevi, S. K. Pushpan and M. Ravikumar, *Angew. Chem., Int. Ed. Engl.*, 1997, **36**, 2598–2601.
28 A. Kalaiselvan, I. S. V. Krishna, A. P. Nambiar, A. Edwin, V. S. Reddy and S. Gokulnath, *Org. Lett.*, 2020, **22**, 4494–4499.
29 S. Luikham and J. Bhattacharyya, *DNA Cell Biol.*, 2022, **41**, 91–102.
30 A. P. Nambiar, P. Nag, R. M. Ipe, S. R. Vennapusa and S. Gokulnath, *Angew. Chem., Int. Ed.*, 2023, **62**, e202306566.
31 J. M. Lintuluoto, K. Nakayama and J. Setsune, *Chem. Commun.*, 2006, 3492–3494.